ACS NANO

www.acsnano.org

ARTICLE

Phase Engineering Modulates the Electronic Structure of the IrO_2/MoS_2 Heterojunction for Efficient and Stable Water Splitting

Shougang Sun, Ziqi Wan, Yingying Xu, Xuemei Zhou,* Wei Gao,* Jinjie Qian, Jie Gao, Dong Cai, Yongjie Ge, Huagui Nie, and Zhi Yang*

Cite This: https://doi.org/10.1021/acsnano.4c18288

Read Online

ACCESS | Metrics & More | Article Recommendations | Supporting Information

ABSTRACT: The engineering of dual-functional catalytic systems capable of driving complete water dissociation in acidic environments represents a critical requirement for advancing proton exchange membrane electrolyzer technology, yet significant challenges remain. In this work, we investigate an $IrO_2/MoS_2/CNT$ heterostructure catalyst demonstrating enhanced bifunctional performance for both the oxygen evolution reaction (OER) and hydrogen evolution reaction (HER) under acidic conditions. Strategic incorporation of IrO_2 into the MoS_2/CNT heterojunction induces a partial phase transformation from 2H to the metastable 1T configuration in MoS_2, thereby modulating the electronic structure of IrO_2 and improving the catalytic performance for overall water splitting. The optimized $IrO_2/MoS_2/CNT$ catalyst exhibited exceptional overpotentials of 9 mV (HER) and 182 mV (OER) at a current density of 10 mA cm^{-2} in acidic media. Full-cell evaluations further confirmed its practical potential, showing a 1.47 V operation voltage that outperforms standard Pt/C||IrO_2 counterparts by 120 mV. The experimental results revealed that the n−n heterojunction between IrO_2/CNT and MoS_2/CNT generates a built-in electric field, enhancing charge redistribution and electron transport. Moreover, density functional theory simulations further identify iridium centers as dominant catalytic loci, with a metastable 1T-MoS_2 phase mediating charge equilibration at atomic interfaces. This modification facilitates *OH adsorption and *OOH deprotonation and lowers the kinetic barrier during the water-splitting process.

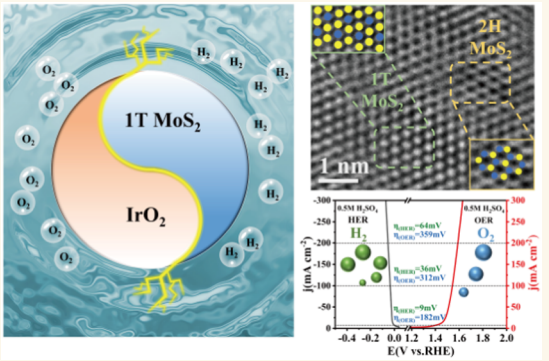

1. INTRODUCTION

Advancing efficient and scalable water-splitting systems represents a critical pathway for tackling pressing global energy demands and environmental sustainability issues. Proton exchange membrane (PEM) electrolysis has emerged as a pivotal technology for green hydrogen generation due to its superior energy conversion rates, modular architecture, and dynamic operational responsiveness.[1,2] Nevertheless, kinetic limitations in both the anodic oxygen evolution reaction (OER) and cathodic hydrogen evolution reaction (HER) processes continue to hinder progress, necessitating reliance on rare noble metal-based catalysts like IrO_2 and Pt that suffer from supply constraints and high costs.[3] These challenges underscore the urgent need for innovative bifunctional electrocatalyst designs that demonstrate optimized reaction efficiency, economic viability, and acid-stable performance to facilitate modular PEM electrolyzer system development.

Implementing heterojunction structural engineering provides a sophisticated methodology to enhance bifunctional electrocatalytic capabilities and significantly reduce reliance on high-cost metallic components. Recently, MoS_2, a widely studied transition metal dichalcogenide, has shown great potential as an HER catalyst due to its earth abundance, tunable electronic structure, and high catalytic activity. In its natural state, MoS_2 typically exists in the semiconducting 2H phase, which exhibits limited HER activity due to poor conductivity and insufficient active sites.[4] Interestingly, the metallic 1T phase of MoS_2 demonstrates significantly enhanced conductivity and catalytic activity, improving its catalytic activity.[5−9] Unfortunately, the metastable 1T phase of MoS_2 presents significant synthesis challenges, being neither

Received: December 17, 2024
Revised: March 11, 2025
Accepted: March 12, 2025

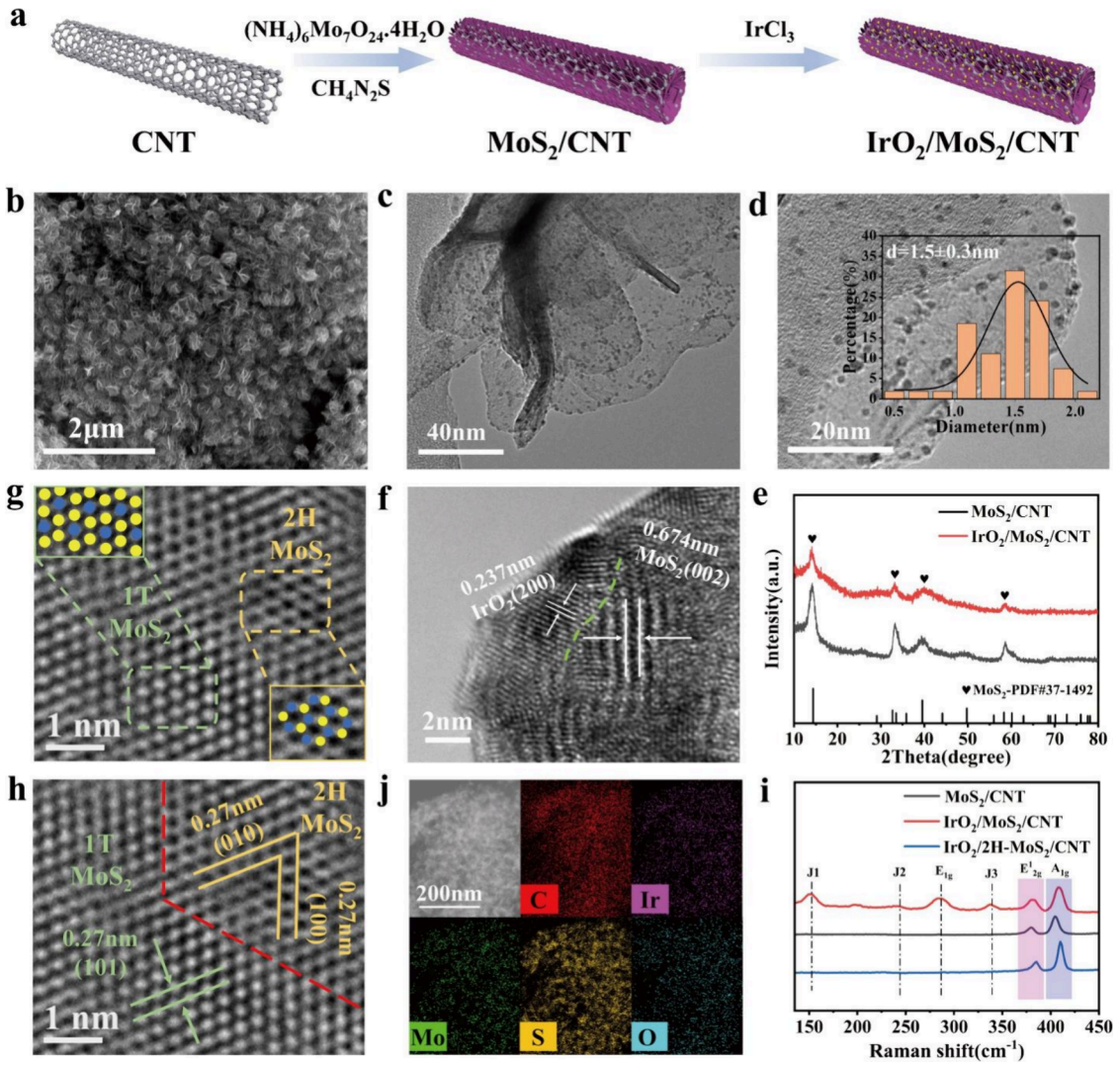

Figure 1. Synthesis and structural characterizations of IrO_2/MoS_2/CNT. (a) Schematic illustration for the preparation of IrO_2/MoS_2/CNT, (b) SEM, (c) TEM, (d) HRTEM, (e) XRD, (f, g and h) TEM, (i) Raman spectra of MoS_2/CNT, IrO_2−MoS_2/CNT and IrO_2/2H-MoS_2/CNT. (j) STEM images of IrO_2/MoS_2/CNT.

naturally obtainable nor readily producible at scale through conventional chemical or physical synthesis routes.[10,11]

Herein, we report the construction of an IrO_2/MoS_2/CNT heterojunction, where the phase of MoS_2 is partially transformed from the 2H phase to the 1T phase. The introduction of IrO_2 not only provides highly active sites for the OER but also facilitates the phase transition of MoS_2 through strong interfacial interactions. Additionally, carbon nanotubes (CNTs) are incorporated to enhance the overall conductivity and structural stability of the heterojunction. The synergistic effect between IrO_2 and 1T MoS_2, combined with the conductive CNT network, enables efficient charge redistribution and electron transfer, thereby significantly improving the bifunctional activity for both HER and OER. The optimized IrO_2/MoS_2/CNT catalyst achieved remarkable performance with low overpotentials of 9 mV (HER) and 182 mV (OER) at 10 mA cm^{-2} under an acidic environment, while requiring only 1.47 V to drive 10 mA cm^{-2} in a two-electrode configuration, outperforming commercial Pt/C||IrO_2 counterparts by 120 mV in cell voltage. Combining the experimental and DFT results demonstrated that Ir sites function as primary active centers, with 1T-MoS_2 enhancing charge redistribution and interfacial structure to promote *OH adsorption, *OOH deprotonation, and lower kinetic barriers during water splitting.

2. RESULTS AND DISCUSSION

2.1. Preparation and Characterization of IrO_2/MoS_2/CNTs. The synthesis procedure for the IrO_2/MoS_2/CNT heterostructure is schematically depicted in Figure 1a. Briefly, the heterostructure IrO_2/MoS_2/CNT is prepared via a two-step hydrothermal method. Initially, MoS_2/CNT composites were synthesized by reacting molybdic acid with thiourea in the presence of carbon nanotubes at 180 °C for 24 h. Subsequent incorporation of $IrCl_3\cdot xH_2O$ into the above precursor followed by thermal treatment at 100 °C for 10 h, marked as IrO_2/MoS_2/CNT. Morphological characterization via scanning electron microscopy (SEM) revealed that the IrO_2/MoS_2/CNT (Figure 1b) composite maintains the nanosheet architecture inherited from its MoS_2/CNT precursor (Figure S1a). Transmission electron microscopy (TEM) analysis (Figure 1c) further demonstrated the homogeneous dispersion of IrO_2 nanoparticles within the matrix, exhibiting an average particle size of 1.5 nm (Figure 1d), compared with the MoS_2/CNT precursor (Figure S1b)

https://doi.org/10.1021/acsnano.4c18288
ACS Nano XXXX, XXX, XXX−XXX

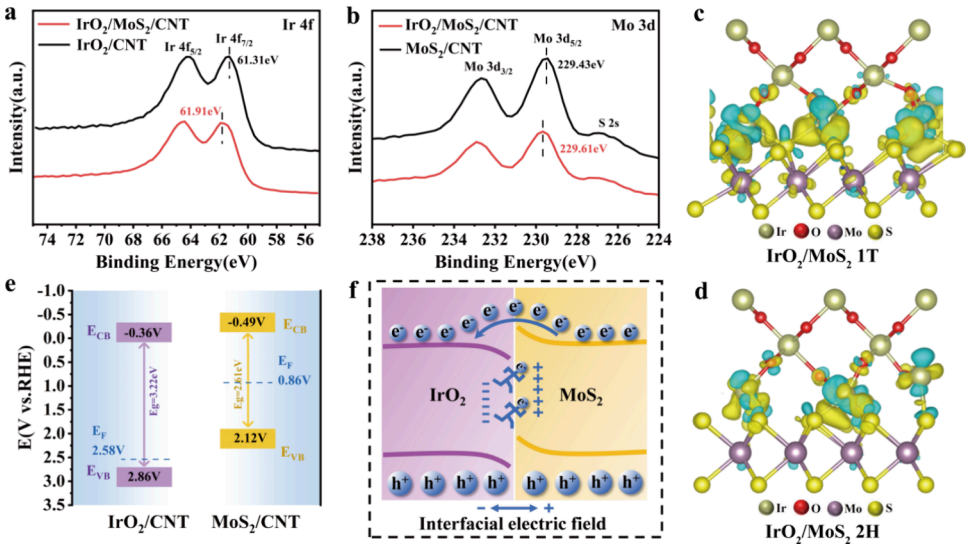

Figure 2. (a) XPS spectra of Ir 4f of the IrO_2/MoS_2/CNT and IrO_2/CNT; (b) XPS spectra of Mo 3d of the IrO_2/MoS_2/CNT and MoS_2/CNT; the distribution of the IrO_2/MoS_2 1T (c) and IrO_2/MoS_2 2H (d); (e) energy band structure alignments of IrO_2/CNT and MoS_2/CNT; and (f) schematic of the interface electronic structure in the IrO_2/MoS_2/CNT heterojunction.

and IrO_2/CNT with uneven particles (Figure S2). The crystalline phase of the IrO_2/MoS_2/CNT heterostructures was characterized using X-ray diffraction (XRD). The XRD pattern confirmed the preservation of MoS_2's hexagonal crystal structure (PDF#37−1492) in the IrO_2/MoS_2/CNT composite (Figure 1e).[5] However, the absence of distinct IrO_2 diffraction peaks suggested effective nanoparticle dispersion and subcritical crystallite dimensions below XRD detection limits, as evidenced by comparison with IrO_2/CNT reference samples (Figure S3). High-resolution TEM (HRTEM) imaging further confirmed the measured interplanar spacings of 0.237 and 0.674 nm correspond to the (200) facets of rutile IrO_2 and (002) facets of MoS_2 in IrO_2/MoS_2/CNT heterojunction (Figure 1f).[5,12] Interestingly, two distinct lattice structures were observed: hexagonal lattice regions with ∼0.27 nm spacing (corresponding to (100)/(010) planes of 2H-phase MoS_2) and trigonal lattice regions with 0.27 nm fringe spacing (attributed to (101) facets of 1T-phase MoS_2),[5,13] as given in typical HRTEM images (Figure 1g,h), indicating that the original 2H MoS_2 is partially converted to 1T MoS_2 following IrO_2 introduction.

The coexisting 1T and 2H MoS_2 phases in the IrO_2/MoS_2/CNT heterostructures were further confirmed by Raman spectroscopy. The Raman spectrum showed three distinct signals at 150 cm^{-1} (J_1), 218 cm^{-1} (J_2), and 327 cm^{-1} (J_3), corresponding to the S−Mo−S bond vibrations in the 1T-MoS_2 phase (Figure 1i), according to previous reports on 1T MoS_2.[5,14] These peaks were absent in the Raman spectra of the 2H MoS_2/CNT and IrO_2/2H-MoS_2/CNT (synthesized by the physical mixing method), clearly indicating the successful stabilization of the metastable 1T phase of MoS_2 within the heterostructure. The elemental distribution within the IrO_2/MoS_2/CNT heterostructure was further characterized by scanning transmission electron microscopy (STEM) elemental mapping (Figure 1j). The elemental maps demonstrated a uniform spatial distribution of C, Mo, Ir, O, and S components across the heterostructure, confirming structural homogeneity and compositional integration. These collective findings confirm the successful formation of coexisting 1T and 2H-MoS_2 phases in the IrO_2/MoS_2/CNT heterostructures achieved through IrO_2 incorporation.

The chemical state and atomic structure of the heterostructured IrO_2/MoS_2/CNT composite were explored by XPS.[12,15,16] The XPS survey for the IrO_2/MoS_2/CNT (Figure S4) indicates the presence of Ir, Mo, O, C and S. Compared to IrO_2/CNT, IrO_2/MoS_2/CNT of the Ir 4f peak is positively shifted by 0.6 eV (Figure 2a); on the other hand, the Mo $3d_{5/2}$ and Mo $3d_{3/2}$ signal in the IrO_2MoS_2/CNT heterostructures exhibited a 0.18 eV positive shift relative to the bare MoS_2/CNT (Figure 2b), indicating strong electronic interactions between IrO_2 and MoS_2, which confirm heterostructure interface formation.

Differential charge density analysis further revealed electron accumulation (yellow regions) and depletion (blue regions) patterns. As illustrated in Figure 2c, notable charge accumulation at the MoS_2 interface suggests electron transfer from IrO_2 to MoS_2, compared to the IrO_2/MoS_2 2H model (Figure 2d). The Bader charge values for the Ir atom in the IrO_2/MoS_2 1T structure were determined to be 8.32 e (Table S1), confirming significant electron transfer from IrO_2 to MoS_2 and highlighting charge redistribution within the IrO_2/MoS_2 system.[17−20] The constructed IrO_2/MoS_2 catalyst achieved charge density redistribution through phase interface engineering with electron-deficient Ir surface sites serving as active centers. This configuration effectively modulates intermediate adsorption behavior and reduces reaction barriers.

The electron transfer at the IrO_2/MoS_2/CNT heterojunction interface was comprehensively investigated through UV−vis spectroscopy (Figure S5a), Mott−Schottky plots, and valence band characterization.[21−23] The optical band gap energy (E_g) was calculated using the fundamental equation:

$$(\alpha h\nu)^n = k(h\nu - E_g)$$

in which $h\nu$ represents photoenergy, α denotes the absorption coefficient, and k is a material-dependent constant. The band gap energies of IrO_2/CNT and MoS_2/CNT were calculated as 3.22 and 2.61 eV, respectively (Figure S5b).

The Mott−Schottky plots in Figure S6 reveal that both IrO_2/CNT and MoS_2/CNT exhibit characteristic n-type

https://doi.org/10.1021/acsnano.4c18288
ACS Nano XXXX, XXX, XXX−XXX

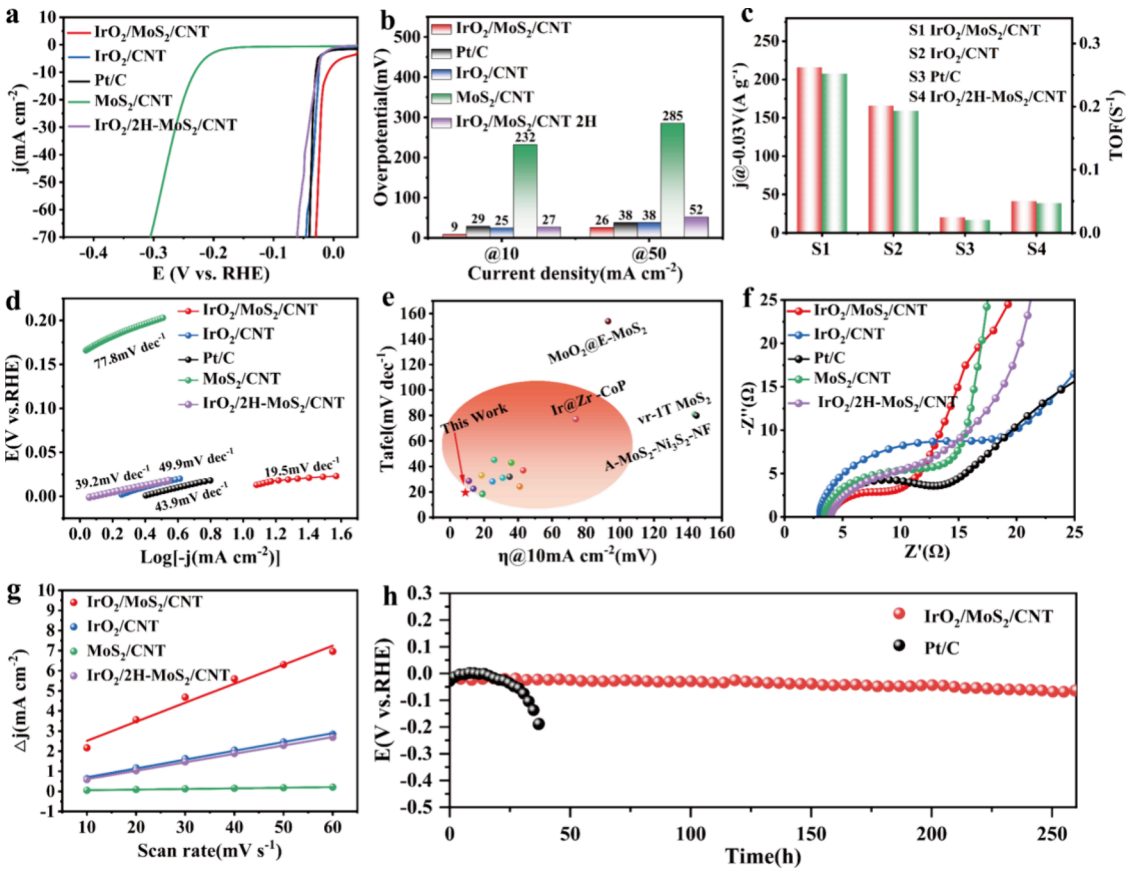

Figure 3. (a) LSV curves of as-grown catalysts in 0.5 M H_2SO_4; (b) Relationship between overpotential and the catalysts with different current density; (c) Mass activity of different catalysts at −0.03 V and TOF at the overpotential of 30 mV; (d) Tafel plots calculated from Figure 3a; (e) Comparison of Tafel slope and overpotentials at the current density of 10 mA cm^{-2} between IrO_2/MoS_2/CNT and recently reported Mo-based electrocatalysts; (f) Nyquist plots for the different electrodes; (g) Charging current density differences plotted versus scan rate; (h) Long-term electrochemical stability of IrO_2/MoS_2/CNT and Pt/C was measured at the current density of 10 mA cm^{-2}.

semiconductor behavior, evidenced by their positive linear slopes.[21,22] The flat band (E_{fb}) potentials were measured at −0.59 V (IrO_2/CNT) and −0.72 V (MoS_2/CNT) vs Ag/AgCl. The conduction band (CB) minimum positions were established at −0.36 vs reversible hydrogen electrode (RHE) for IrO_2/CNT and −0.49 V vs RHE for MoS_2/CNT, consistent with n-type semiconductor behavior. The valence band (VB) maxima were determined to be 2.86 and 2.12 V vs RHE for IrO_2/CNT and MoS_2/CNT, respectively, through the combined band gap and electrochemical analysis. Energy band diagrams (Figure 2e) were constructed using the established $E_g = E_{CB} - E_{VB}$, illustrating the relative band positions of IrO_2/CNT and MoS_2/CNT. Valence band XPS measurements (Figure S7) revealed Fermi level positions at 2.58 eV for IrO_2/CNT and 0.86 eV for MoS_2/CNT relative to their valence band maxima. Heterojunction formation enables spontaneous electron migration from the higher-Fermi-level MoS_2/CNT component to the lower-Fermi-level IrO_2/CNT. This interfacial charge transfer triggers band bending and spatial charge redistribution, as depicted in Figure 2f.

The above results, combined with the HRTEM image of IrO_2/MoS_2/CNT in Figure1f, confirm the successful formation of an n−n heterojunction structure in IrO_2/MoS_2/CNT. The established heterojunction between IrO_2/CNT and MoS_2/CNT generates a built-in electric field that enhances charge carrier mobility across the interface. The surface potential modification creates positive charge centers on IrO_2/CNT, promoting OH^- species electron donation. The transferred electrons subsequently undergo recombination with valence band hole carriers within the IrO2/CNT lattice, facilitated by the heterojunction-induced charge compensation mechanism. The optimized interfacial electronic structure significantly improves the charge transfer kinetics and modifies the surface electronic configuration, thereby enhancing the electrocatalytic activity of the IrO_2/MoS_2/CNT material for water splitting.

2.2. Catalytic Activity for HER and OER. The electrocatalytic performance of the IrO_2/MoS_2/CNT catalyst for both HER and OER was systematically investigated in 0.5 M H_2SO_4 with a three-electrode configuration. The HER activity was evaluated through linear sweep voltammetry (LSV) measurements. The IrO_2/MoS_2/CNT catalyst exhibited enhanced HER activity compared to bare MoS_2/CNT and IrO_2/CNT (Figures 3a and S8). The optimal IrO_2/MoS_2/CNT catalyst showed small overpotentials of 9 and 26 mV at current densities of 10 and 50 mA cm^{-2}, respectively, outperforming commercial Pt/C catalyst (29 and 38 mV), as given in Figures 3b and S9. As the current density increased, the IrO_2/MoS_2/CNT catalyst maintained a greater advantage in terms of low overpotential compared with the other samples. In comparison, the catalysts synthesized by the physical mixing method, namely, the IrO_2/2H-MoS_2/CNT, exhibited lower catalytic performance compared to the IrO_2/MoS_2/CNT with the 1T-2H phase, suggesting enhanced electronic structure modulation through phase engineering, thereby enhancing the

https://doi.org/10.1021/acsnano.4c18288
ACS Nano XXXX, XXX, XXX−XXX

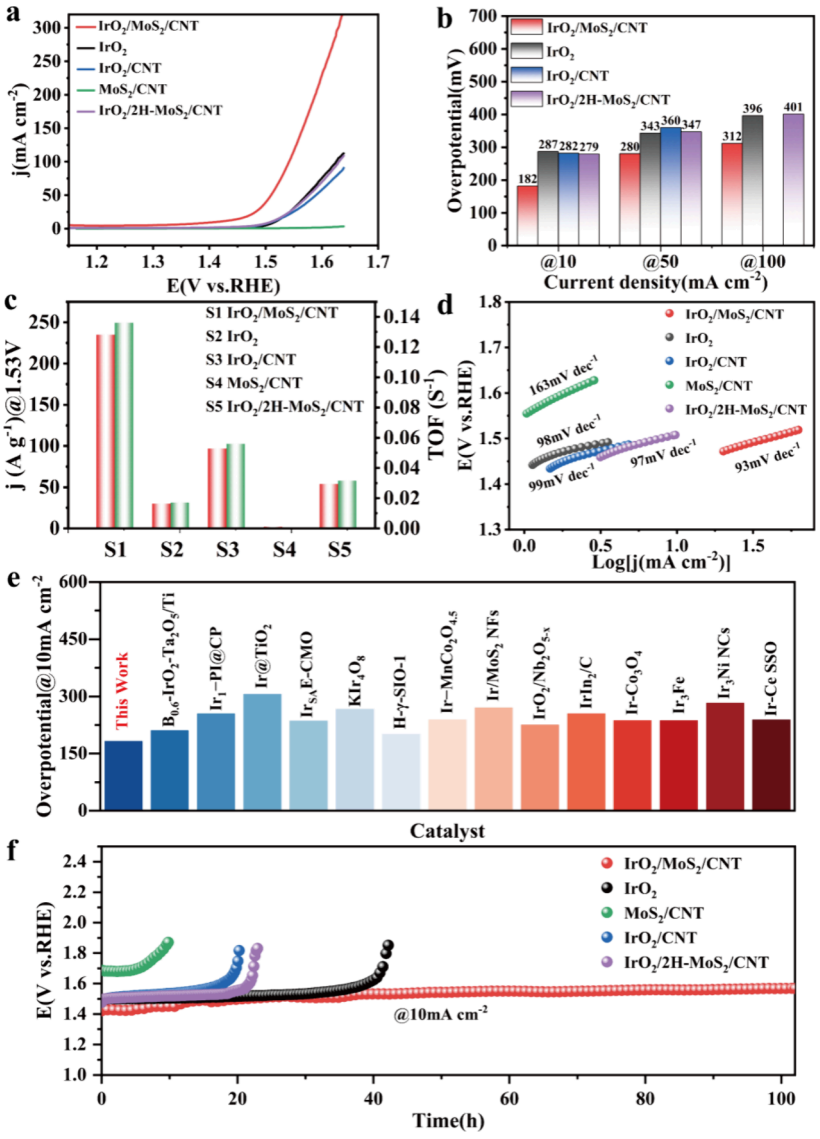

Figure 4. (a) LSV curves for different catalysts with 90%-*iR* correction in acid medium; (b) relationship between overpotential and the catalysts with different current density; (c) mass activity of different catalysts at 1.53 V and TOF at the overpotential of 300 mV; (d) Tafel plots calculated from Figure 2a; (e) comparison of overpotentials at the current density of 10 mA cm^{-2} between IrO_2/MoS_2/CNT and recently reported Ir-based electrocatalysts; (f) long-term electrochemical stability test was measured at the current density of 10 mA cm^{-2}.

activity and kinetic performance of the catalyst. Mass activity measurements at −0.03 V vs RHE showed IrO_2/MoS_2/CNT achieving 216 A g^{-1}, representing 10.8-fold and 5.2-fold improvements over Pt/C (20 A g^{-1}) and IrO_2/2H-MoS_2/CNT (41.2 A g^{-1}) electrodes, respectively (Figure 3c). The turnover frequency (TOF) of the IrO_2/MoS_2/CNT catalyst was 0.252 s^{-1} at 30 mV overpotential, exceeding Pt/C (0.02 s^{-1}) and IrO_2/2H-MoS_2/CNT (0.047 s^{-1}) by factors of 12.6 and 5.4, respectively, evidencing optimized catalytic site exposure efficiency and enhanced fundamental catalytic performance. Tafel slope analysis revealed accelerated HER kinetics with IrO_2/MoS_2/CNT (19.5 mV dec^{-1}), significantly lower than that with MoS2/CNT (77.8 mV dec^{-1}), IrO2/CNT (49.9 mV dec^{-1}), and Pt/C (43.9 mV dec^{-1}), as depicted in Figure 3d. In fact, the catalytic activities of the as-fabricated IrO_2/MoS_2/CNT catalyst are comparable with recently reported analogous electrocatalysts in acid electrolytes,[24−26] as presented in Figure 3e and Table S2.

These HER performance enhancements were quantitatively validated through complementary electrochemical impedance spectroscopy (EIS) and electrochemically active surface area (ECSA) analyses. Evidently, the Nyquist plot of IrO_2/MoS_2/CNT heterostructures exhibits the smallest semicircle diameter among all of the tested electrodes, suggesting minimal interfacial charge transfer resistance (Figure 3f). Meanwhile, the contact angle between water and IrO_2/MoS_2/CNT heterostructures showed an anticipated decrease compared with 2H MoS_2/CNT and IrO_2/CNT, because of the good hydrophilicity of 1T MoS_2 (Figure S10). This enhanced wettability promotes optimal electrolyte-catalyst interfacial contact while maximizing the active site accessibility. To further analyze the intrinsic catalytic activity, CV-based ECSA evaluation (Figure S11) revealed superior active site exposure in IrO_2/MoS_2/CNT, as evidenced by its steeper linear fitting slope compared to control samples (Figure 3g).

Besides its high activity and fast kinetics, the IrO_2/MoS_2/CNT heterostructure also demonstrated remarkable opera-

https://doi.org/10.1021/acsnano.4c18288
ACS Nano XXXX, XXX, XXX−XXX

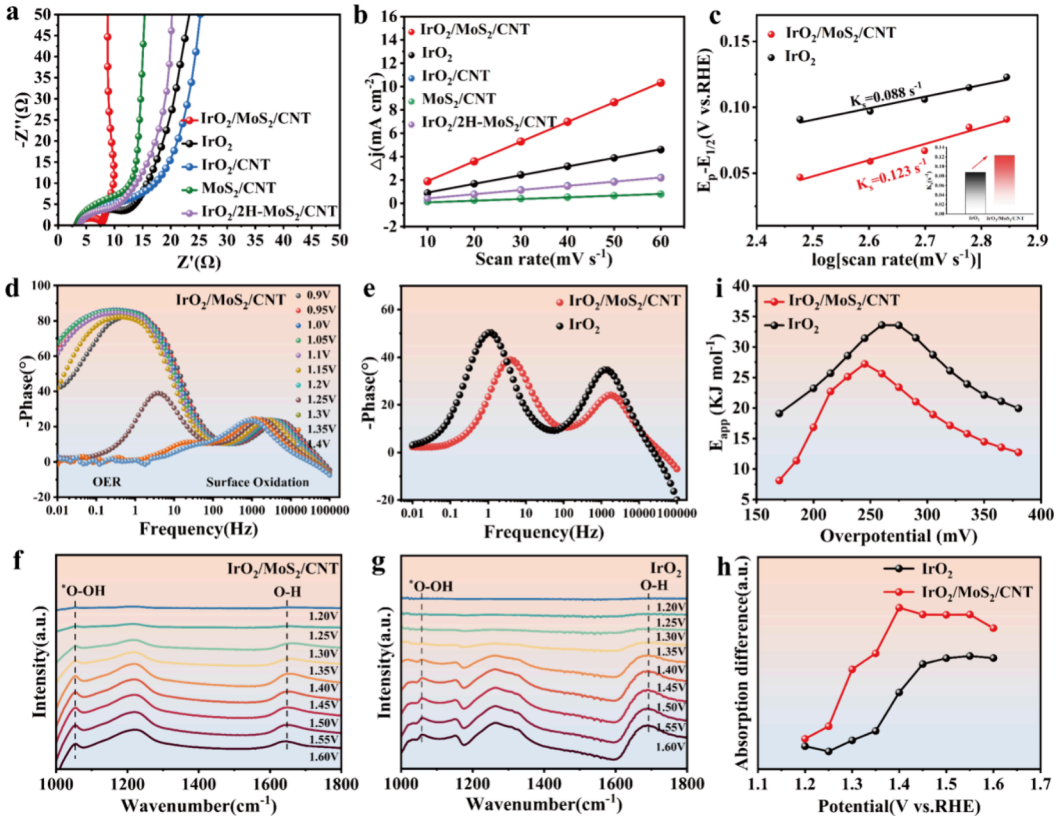

Figure 5. (a) EIS curves; (b) Charging current density differences plotted versus scan rate. (c) Ks of IrO_2/MoS_2/CNT and IrO_2; (d) Bode phase plots for IrO_2/MoS_2/CNT catalysts at different applied potentials versus SCE. in 0.5 M H_2SO_4; (e) Bode phase plots of pure IrO_2/MoS_2/CNT and IrO_2 at 1.3 V vs SCE. In situ FTIR spectra of IrO_2/MoS_2/CNT (f) and IrO_2 (g); (h) Peak intensity enhancements of the absorption bands at 1055 cm^{-1} as a function of applied potential; (i) Arrhenius plots of the kinetic current illustration of different activation energy of OER at 1.5 V versus RHE for IrO_2/MoS_2/CNT and IrO_2.

tional stability in acid media, maintaining negligible potential deviation during prolonged operation at 10 mA cm^{-2} for 200 h (Figure 3h). Conversely, the Pt/C catalyst showed a sharp potential decrease within the initial 40 h range. Additionally, stepwise chronopotentiometric testing of the IrO_2/MoS_2/CNT electrode was conducted across current densities spanning 10−50 mA cm^{-2} (Figure S12). Remarkably, the IrO_2/MoS_2/CNT electrode exhibited complete potential recovery to baseline values at 10 mA cm^{-2} following high-current-density operation. This behavior highlights the mechanical robustness and stability of the IrO_2/MoS_2/CNT electrode under dynamic operating conditions.

The OER evaluation in 0.5 M H_2SO_4 revealed enhancement trends analogous to those of HER performance (Figure S13). Among the LSV curves shown in Figure 4a, for the OER process, the IrO_2/MoS_2/CNT electrocatalysts exhibited significantly higher electrocatalytic activities compared with other electrocatalysts. The IrO_2/MoS_2/CNT heterostructure exhibited superior electrocatalytic performance with an overpotential of 182 mV at 10 mA cm^{-2}, demonstrating significant advantages over both IrO_2/2H-MoS_2/CNT (279 mV) and commercial IrO_2 catalysts (287 mV). This performance gap became even more pronounced at elevated current densities, where the IrO_2/MoS_2/CNT heterostructure maintained a low overpotential of 312 mV at 100 mA cm^{-2}, outperforming its 2H-phase counterpart (401 mV) and commercial IrO_2 (396 mV) by substantial margins, as illustrated in Figure 4b.

Mass activity analysis revealed 235 A g^{-1} at 1.53 V vs RHE for IrO_2/MoS_2/CNT catalyst, representing approximately 7.9-fold and 4.4-fold improvements over commercial IrO_2 (29.8 A g^{-1}) and IrO_2/2H-MoS_2/CNT electrodes (54 A g^{-1}), respectively (Figure 4c). TOF calculations at 300 mV overpotential showed 0.136 s^{-1} for IrO_2/MoS_2/CNT, exceeding 8-fold and 4.3-fold improvements over commercial IrO_2 (0.017 s^{-1}) and IrO_2/2H-MoS_2/CNT (0.0315 s^{-1}) respectively, confirming superior atomic-level efficiency in oxygen evolution catalysis. The catalytic enhancement of IrO_2/MoS_2/CNT was quantitatively confirmed through Tafel analysis, recording a 93 mV dec^{-1} slope that demonstrates accelerated oxygen evolution kinetics compared to those of commercial IrO_2 electrodes (Figure 4d). These results suggest that the 1T-2H phase of IrO_2/MoS_2/CNT facilitates efficient water adsorption and improves reaction kinetics due to its electronic structure rearrangement and enhanced hydrophilicity. At 10 mA cm^{-2}, the IrO_2/MoS_2/CNT exhibited overpotentials competitive with or superior to reported high-performance Ir-based catalysts, as validated by comparative literature analysis (Figure 4e and Table S3).[27−30] Furthermore, the IrO_2/MoS_2/CNT catalyst demonstrated exceptional stability, maintaining performance at 10 mA cm^{-2} for 100 h, outperforming other catalysts (Figure 4f).

2.3. Revealing the Origin of OER Activity. The enhanced OER activity of IrO_2/MoS_2/CNT was systematically investigated by using comprehensive electrochemical characterizations. First, Nyquist plots from EIS at open-circuit potential revealed the IrO_2/MoS_2/CNT electrode exhibiting

https://doi.org/10.1021/acsnano.4c18288
ACS Nano XXXX, XXX, XXX−XXX

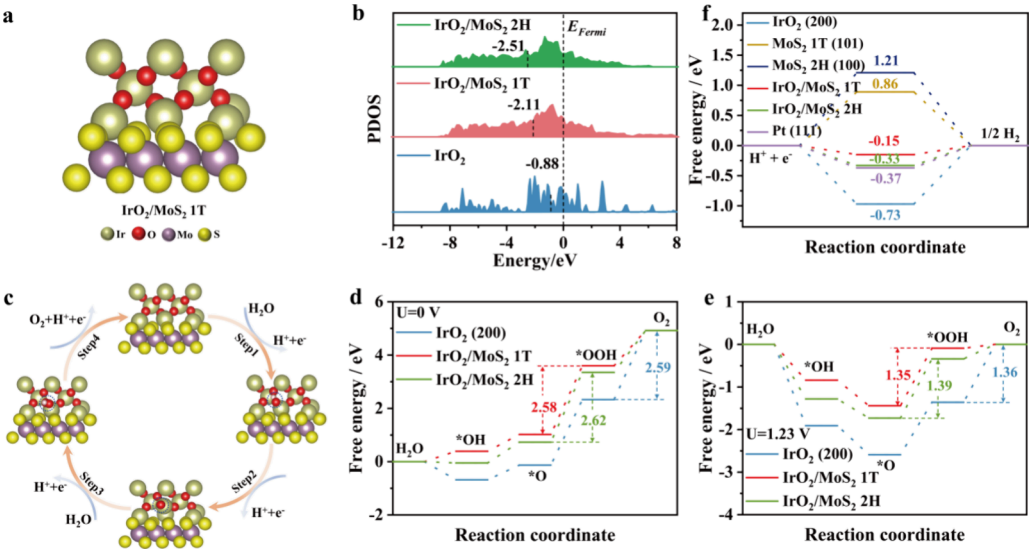

Figure 6. (a) Structure model of IrO_2/MoS_2 1 T; (b) PDOS of different catalysts; (c) key intermediate adsorption configuration models for the Ir site of IrO_2/MoS_2 1 T; (d and e) computed overpotential versus different catalysts for OER at U = 0 and U = 1.23 V; (f) Computed overpotential versus different catalysts for HER.

the smallest charge-transfer impedance and largest Warburg impedance among tested catalysts (Figure 5a).[31] This indicates optimized electron transfer kinetics and enhanced mass transport properties, which can be attributed to the synergistic 2H-1T phase transition-induced electronic modulation in MoS_2. Next, the ECSA was evaluated via double-layer capacitance (C_{dl}) according to CVs (Figure S14). The slope of the linear fit for the IrO_2/MoS_2/CNT electrode was steeper compared to the other electrodes (Figure 5b), indicating that the IrO_2/MoS_2/CNT electrode possesses superior active site exposure.

The OER reactivity is governed by optimal adsorption energetics of oxygenated intermediates (OH*, O*, OOH*) at catalytic metal centers.[32] Laviron analysis quantified *OH binding affinity at Ir active sites in IrO_2/MoS_2/CNT versus commercial IrO_2.[16] Linear correlation between anodic peak currents and the square root of the CVs scan rate confirmed diffusion-controlled *OH adsorption kinetics (Figure S15). The calculated rate constant (K_s) for IrO_2/MoS_2/CNT was 0.123 s^{-1}, which is higher than that of commercial IrO_2 (0.088 s^{-1}), as quantified in Figure 5c. This enhanced kinetic parameter confirms stronger *OH intermediate stabilization at the interfacial active sites of IrO_2/MoS_2/CNT. Competitive methanol oxidation assays probed OH*/O* binding energetics in IrO_2/MoS_2/CNT, further revealing optimized intermediate-specific adsorption through electrophilicity-dependent competitive adsorption (Figure S16).[33]

Mechanistic investigation of oxygen evolution kinetics employed operando electrochemical impedance spectroscopy to track oxygenated intermediate adsorption dynamics on the IrO_2/MoS_2/CNT during catalytic operation. Figures 5d and S17 showcase characteristic interfacial responses through Nyquist and Bode phase plots recorded under operando conditions (0.9−1.4 V vs SCE), benchmarked against pure IrO_2 (Figure S18). At 1.25 V, the Bode phase plots showed that the low-frequency interfacial signature of IrO_2/MoS_2/CNT had reduced phase angles and characteristic frequency shift compared to IrO_2 (Figure 5e), indicating faster deprotonation of *OOH intermediates.[34,35]

To further investigate the catalytic mechanism, operando FTIR spectroscopy employing a specialized electrochemical cell tracked oxygen intermediate evolution during catalysis.[36,37] Figure 5f presents potential-dependent FTIR spectra for IrO_2/MoS_2/CNT, revealing a band in the range of 1600−1800 cm^{-1} corresponding to the H−O−H bending mode (δH−O−H) of water. Progressive potential application induced a characteristic 1055 cm^{-1} vibration signature in IrO_2/MoS_2/CNT, diagnostic of *OOH intermediate formation during the process of acidic OER.[36] Control experiments with pure IrO_2 showed no detectable features in the 1000−1100 cm^{-1} range (Figure 5g). This spectroscopic verification confirms that IrO_2/MoS_2/CNT heterointerface engineering enhances $4e^-$ pathway selectivity while stabilizing critical oxygen intermediates. Potential-dependent intensification of the 1055 cm^{-1} vibrational mode (Figure 5h) quantitatively tracks *OOH accumulation dynamics during the OER operation. Notably, oxygen coupling events preceding *OOH formation were detected at 1.25 V, indicating sequential intermediate transformation kinetics in the catalytic cycle. Furthermore, complementary rotating ring-disk electrode (RRDE) analysis demonstrated minimal peroxide byproduct formation, confirming that the IrO_2/MoS_2/CNT electrode predominantly followed 4-electron pathway selectivity through RRDE quantification, as shown in Figure S19.[38] This mechanistic synergy between thermodynamic *OOH stabilization and kinetic oxygen coupling enables optimized four-electron pathway efficiency and enhanced reaction kinetics in acidic media.[37]

The experimental conclusions received additional substantiation through analysis of the derived activation energy (E_a) values.[16,39] Kinetic studies under varying temperature conditions were conducted for IrO_2/MoS_2/CNT and IrO_2 electrodes to establish their respective E_a values during the acidic OER. LSV measurements of both electrode systems in 0.5 M sulfuric acid electrolyte were obtained across temperatures ranging from 20 to 60 °C (Figure S20). Consistent with thermodynamic principles, both catalytic systems demonstrated progressively enhanced activity with rising operational temperatures. Through the application of the Arrhenius

https://doi.org/10.1021/acsnano.4c18288
ACS Nano XXXX, XXX, XXX−XXX

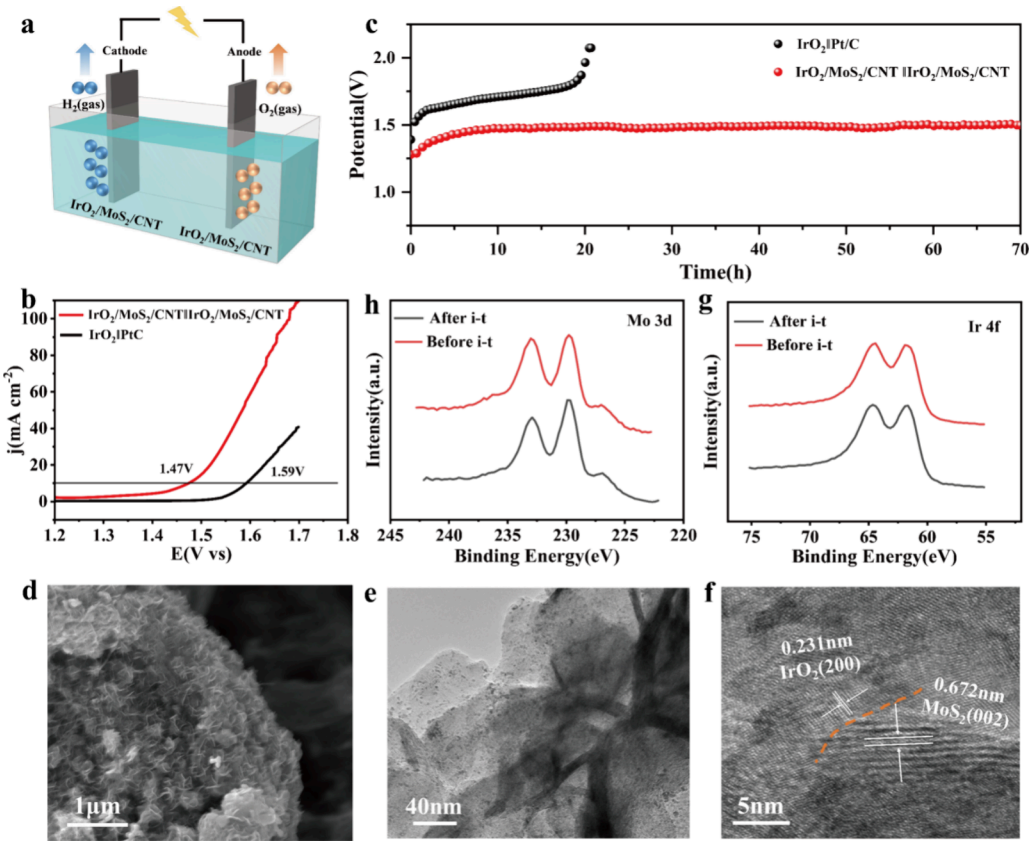

Figure 7. (a) Acid electrolyzer using two identical IrO_2/MoS_2/CNT as both the cathode and anode; (b) LSV curves using IrO_2/MoS_2/CNT as two electrodes; (c) chronopotentiometric response curve of IrO_2/MoS_2/CNT at 10 mA cm^{-2}; SEM (d) and TEM images (e, f) and XPS (g, h) of IrO_2/MoS_2/CNT after the stability test.

relationship, activation energy values at 1.5 V versus RHE were determined as shown in Figure 5i. The calculated E_a for the IrO_2/MoS_2/CNT electrode measured 23.4 kJ mol^{-1}, exhibiting a substantial reduction compared to that of pure IrO_2 (33.6 kJ mol^{-1}). This energy differential suggests significantly diminished kinetic barriers in the OER process resulting from structural phase modifications. The reduced activation energy conclusively validates the enhanced oxygen evolution reaction efficiency exhibited by the IrO_2/MoS_2/CNT catalytic system.

2.4. Mechanism Investigation by Density Functional Theory Calculation. Based on the experimental findings, correlative optimized theoretical models were constructed, including IrO_2 (200), MoS_2 1T (101), MoS_2 2H (100), IrO_2/MoS_2 1T and IrO_2/MoS_2 2H (Figures 6a, S21−S27 and the details regarding the selection of the optimal model are provided in the Supporting Information). Interface electronic interactions were analyzed through d-band center theory, where the proximity of metallic d-orbital centers to Fermi levels typically strengthens intermediate adsorption.[40] However, the Sabatier principle dictates that optimal catalytic interfaces require moderated bonding strength, and excessive or insufficient interactions impair reaction dynamics.[41] Projected density of states (PDOS) calculations demonstrated progressive d-band center displacement from −0.88 eV (IrO_2/CNT) to −2.51 eV (IrO_2/MoS_2 2H), then to −2.11 eV (IrO_2/MoS_2 1T) (Figure 6b), confirming the electronic modulation effect of MoS_2 on IrO_2. Previous studies associate downward-shifted d-band centers with enhanced H_2O adsorption/dissociation capabilities, improving electrolytic kinetics for water splitting.[42,43] Therefore, the intermediate d-band position in IrO_2/MoS_2 1T suggests superior water-splitting functionality compared to MoS_2 2H on the catalytic surface.

We further examined the effects of different MoS_2 phases on the OER catalytic thermodynamics. The geometric configurations of reactive intermediates and associated energy landscapes are detailed in Figures 6c−e and S28. As illustrated in Figure 6d, all four elementary steps (Ir acting as active sites) exhibit uphill free energy changes under the equilibrium conditions (U = 0 V). Notably, the oxygen evolution bottleneck in IrO_2 (200) occurs during OOH* to O_2 conversion, exhibiting a 2.59 eV activation barrier - the predominant limitation in acidic OER. Applied potential elevation to 1.23 V, the energy barrier of the rate-determining step (RDS) decreases significantly to 1.36 eV (Figure 6e). Upon introduction of IrO_2 into MoS_2, the conversion of OOH* to O_2 for IrO_2/MoS_2 1T demonstrates a much lower overpotential of 1.06 eV (U = 0 V), which further decreases to 0.09 eV at the operational potential. Phase-dependent mechanistic shifts emerge: IrO_2/MoS_2 1T and IrO_2/MoS_2 2H systems transition their rate-limiting steps to the formation of OOH*, displaying barriers of 2.58/2.62 eV (U = 0 V) and 1.35/1.39 eV (U = 1.23 V), respectively. The 1T-phase composite achieves superior kinetic enhancement in its third reaction step (1.35 eV barrier), representing the lowest activation energy across tested materials. Crucially, the harmonized energy distribution across reaction coordinates in IrO_2/MoS_2 1T promotes both catalytic efficiency and operational stability during prolonged oxygen evolution.

Based on the Sabatier principle, attaining an optimal hydrogen adsorption free energy (ΔG_{H^*}) close to the

https://doi.org/10.1021/acsnano.4c18288
ACS Nano XXXX, XXX, XXX−XXX

theoretical optimum ($\Delta G_{H^*} = 0$ eV) is critical for balancing the H* adsorption and H_2 desorption.[44,45] Analysis of Figures 6f and S29, the 2H phase of MoS_2 demonstrates the highest ΔG_{H^*} value (1.21 eV), reflecting insufficient hydrogen proton adsorption capability at Mo active sites that limits reaction efficiency. The IrO_2-modified 2H-MoS_2 composite shows substantially improved hydrogen adsorption characteristics, with ΔG_{H^*} values reaching −0.33 eV at Ir active sites, while the 1T-phase IrO_2/MoS_2 system achieves a marginally more negative ΔG_{H^*} value of −0.15 eV. These findings indicate that the 1T-phase IrO_2/MoS_2 heterostructure achieves optimal surface adsorption characteristics for hydrogen intermediates, enabling enhanced HER activity through improved reaction kinetics. The enhanced catalytic performance in both oxygen and hydrogen evolution reactions arises from the synergistic combination of IrO_2 and MoS_2 components, interfacial charge redistribution effects, and superior electrical conductivity within the IrO_2/MoS_2/CNTs composite system.

2.5. Overall Water Splitting. Building upon the exceptional bifunctional catalytic performance of IrO_2/MoS_2/CNT in oxygen/hydrogen evolution reactions, we developed an acidic water electrolysis system employing symmetrical IrO_2/MoS_2/CNT electrodes for both the anode and cathode compartments (Figure 7). The water electrolysis performance was evaluated through LSV measurements. As shown in Figure 7b, IrO_2/MoS_2/CNT demonstrated superior activity, requiring only 1.47 V to achieve 10 mA cm^{-2} current density, substantially lower than the 1.59 V required by the IrO_2||Pt/C benchmark system under identical conditions. This performance positions the IrO_2/MoS_2/CNT catalyst as competitive with, and in some cases superior to, recently reported precious metal-based electrocatalysts in overall water splitting efficiency.[46−48] Given the importance of electrode durability for practical water splitting applications, IrO_2/MoS_2/CNT was tested for 70 h at 10 mA cm^{-2} (Figure 7c), during which the cell voltage attenuation is not very noticeable. The nanosheet-like morphology of IrO_2/MoS_2/CNT was well-preserved after prolonged operation, as shown in Figure 7d, further demonstrating the excellent stability of the as-synthesized material. Additionally, HRTEM (Figure 7e,f) and XPS (Figure 7g,h) analyses confirmed that the surface structure remained largely unchanged after the OER stability tests, underscoring the high durability of IrO_2/MoS_2/CNT for water splitting.

3. CONCLUSIONS

In summary, the IrO_2/MoS_2/CNT heterostructure featuring controlled phase conversion of MoS_2 from the thermodynamically stable 2H phase to the catalytically active 1T phase alongside an engineered interfacial potential gradient, was successfully fabricated through sequential hydrothermal synthesis. Electrochemical characterization revealed that the optimized catalyst achieves remarkably low HER and OER overpotentials (9 and 182 mV, respectively) at current densities of 10 mA cm^{-2} in acidic electrolyte conditions. When implemented in a symmetrical electrolyzer configuration, the system required only 1.47 V to reach 10 mA cm^{-2}, representing a 120 mV improvement over the benchmark Pt/C||IrO_2 configuration. Combined experimental characterization and computational modeling identified iridium centers as principal catalytic sites, with the 1T-MoS_2 phase promoting charge redistribution dynamics and interfacial electron transport. This synergistic interaction accelerates hydroxyl intermediate adsorption, optimizes oxygenated species deprotonation pathways, and minimizes activation energy barriers throughout the water dissociation process. The demonstrated phase engineering methodology possesses generalizability potential, establishing a rational design paradigm for developing advanced electrocatalytic systems in renewable energy technologies.

4. EXPERIMENTAL SECTION

4.1. Chemicals. All reagents used were of analytical-grade purity and were employed as received without additional purification steps. The molybdenum precursor (ammonium molybdate tetrahydrate), sulfur source (thiourea), and iridium precursor ($IrCl_3 \cdot xH_2O$) were sourced from Aladdin Biochemical Technology (Shanghai). Commercial catalysts (Pt/C and IrO_2) were acquired from Johnson Matthey. Nafion solution (5% concentration) and anhydrous ethanol were procured from Sigma-Aldrich. The sulfuric acid electrolyte was supplied by Sinopharm Chemical Reagent Co. All aqueous solutions utilized ultrapure water from Thermo Fisher Scientific (USA).

4.2. Preparation of MoS_2/CNT and IrO_2/MoS_2/CNT. The MoS_2/CNT hybrid material was prepared through conventional hydrothermal synthesis following this sequence: Initially, 40 mg of ammonium molybdate and 12 mg of CNTs were dispersed in 10 mL of deionized H_2O under 30 min of ambient agitation. Subsequently, 0.68 g of thiourea was dissolved in 20 mL of aqueous solution, which was then gradually introduced into the molybdenum-containing suspension during 60 min of continuous mixing. The homogeneous mixture underwent hydrothermal treatment in a Teflon-lined autoclave maintained at 180 °C for 24 h. Postreaction purification involved centrifugal separation (8000 rpm, 5 min) followed by sequential ethanol/water rinsing cycles to eliminate ionic residues. Vacuum drying at 60 °C for 12 h yielded the intermediate product, which subsequently underwent pyrolysis at 800 °C (5 °C/min ramp) under argon flow for 2 h to obtain the final MoS_2/CNT composite.

The deposition of IrO_2 nanoparticles onto the MoS_2/CNT substrates was achieved through hydrothermal processing. Precise quantities of the MoS_2/CNT precursor (15 mg) and iridium precursor (8.56 mg $IrCl_3 \cdot xH_2O$) underwent separate dispersion in 15 mL ethanol aliquots through 60 min of ultrasonication and magnetic agitation. The combined suspension was subjected to hydrothermal treatment in a Teflon-lined reactor at 100 °C for 10 h. Postsynthesis processing involved vacuum filtration, solvent rinsing cycles, and final vacuum drying at 60 °C for 12 h to obtain the IrO_2/MoS_2/CNT catalyst.

4.3. Material Characterization. Microstructural characterization was conducted utilizing a JEOL-2100F electron microscope operated at 200 kV acceleration voltage, enabling TEM imaging, HRTEM analysis, and elemental distribution mapping via STEM. Crystalline phase identification was performed using a Rigaku D/MAX-2400 X-ray diffractometer with Cu Kα irradiation (λ = 1.5406 Å) under 40 kV/100 mA operational parameters. Surface chemical states were examined through XPS measurements performed in ultrahigh vacuum conditions with monochromatic Al Kα X-ray excitation (15 kV, 10 mA) and electron energy analysis via a Scienta SES 2002 hemispherical analyzer. Structural fingerprinting was achieved through Raman spectroscopy using a Renishaw in Via system equipped with a 532 nm wavelength excitation source.

4.4. Electrochemical Measurements. Electrochemical characterizations employed a conventional three-electrode configuration using a CHI760E potentiostat (CH Instruments). Catalyst inks were prepared by dispersing 4 mg of active material through ultrasonic homogenization in 1 mL of distilled water, followed by precise deposition (10 μL aliquot) onto a carbon paper substrate. Electrode preparation was completed by applying 5 μL of Nafion binder (0.2% ethanolic solution) after ink drying. All measurements utilized 0.5 M sulfuric acid electrolyte, with recorded potentials converted to the RHE scale using $E_{RHE} = E_{SCE} + 0.264$ V. Catalytic performance evaluation involved LSV (10 mV/s scan rate) for HER/OER characterization under acidic conditions. EIS was acquired across a

https://doi.org/10.1021/acsnano.4c18288
ACS Nano XXXX, XXX, XXX−XXX

0.01−100 kHz frequency spectrum at equilibrium potential. Durability testing comprised 100-h chronopotentiometry at 10 mA cm^{-2} and multistep current density profiling (10−50 mA cm^{-2} increments) for evaluating electrochemical robustness. Full water electrolysis was implemented through a symmetrical cell configuration where IrO_2/MoS_2/CNT functioned as both the anode and cathode. Current−voltage profiles were acquired via LSV (1 mV s^{-1} scan rate) in 0.5 M sulfuric acid electrolyte across a 1.2−1.7 V potential window. All data collection occurred without impedance compensation to preserve the inherent system resistance characteristics. Catalytic overpotentials were calculated through the Tafel formulation following $\eta = a + b \log|j|$, where η (V) quantifies electrode polarization, j (mA cm^{-2}) reflects operational current density, and b (mV dec^{-1}) characterizes reaction kinetics through Tafel slope analysis. ECSA was determined through double-layer capacitance (C_{dl}) measurements using CV across scan rates (10−60 mV s^{-1}) within a non-Faradaic voltage range. C_{dl} values were calculated from the linear regression of capacitive current versus scan rate plots. Turnover frequency (TOF) serves as a fundamental performance indicator for quantifying inherent catalytic efficiency, decoupled from surface area effects. The calculation employs: $\mathrm{TOF} = \frac{|j| A}{mFn}$, in which j represents the current density measured at 300 mV overpotential during LSV testing, A indicates the geometric electrode area (0.071 cm^2), F denotes Faraday's constant (96,485 C mol^{-1}), and n corresponds to active site quantity (mol). The 1/2 factor arises from the two-electron hydrogen evolution pathway, while 1/4 accounts for the four-electron oxygen evolution mechanism.

4.5. Mott−Schottky (MS) Test. Semiconductor characterization employed a three-electrode configuration in 0.2 M Na_2SO_4 aqueous electrolyte, with catalyst-modified indium tin oxide (ITO) used as the working electrode. Catalyst inks were formulated through ultrasonic homogenization (30 min) of 2 mg active material with 100 μL isopropanol and 10 μL Nafion binder. A 40 μL aliquot was deposited onto the ITO substrates (1 cm^2 active area). Vacuum annealing at 60 °C for 12 h achieved electrode stabilization, followed by desiccation storage. Potential values were converted to the RHE scale through $E_{RHE} = E_{Ag/AgCl} + 0.233$. Flat-band potentials and carrier densities were derived from capacitance−potential profiles recorded at a 1 kHz frequency.

4.6. DFT Calculations. First-principles calculations were conducted utilizing the VASP code within a periodic DFT framework.[49] Electron exchange-correlation effects were modeled through the projector augmented wave-projector augmented wave (GGA-PAW) formalism.[50,51] A 15 Å vacuum spacer was incorporated perpendicular to the catalytic surfaces to eliminate periodic interference. Geometry optimizations employed a 400 eV plane-wave cutoff and 2 × 2 × 1 k-point sampling using the Monkhorst−Pack grid methodology.[52] Convergence thresholds were set at $1 \times 1 \times 10^{-5}$ eV for electronic self-consistency and 0.02 eV/Å for ionic force relaxation. Long-range van der Waals interactions were modeled through Grimme's DFT-D3 dispersion correction scheme. Within the computational hydrogen electrode framework, proton−electron pair free energy equivalence to gaseous H_2 was applied.[53] Reaction step energetics were computed as follows:

$$\Delta_G = \Delta_E + \Delta E_{ZPE} - T\Delta S$$

where Δ_E denotes energy differences obtained directly from the DFT simulation, ΔE_{ZPE} represents zero-point vibrational corrections, and entropy contributions (T = 298.15 K) were derived from standard thermodynamic tables.

ASSOCIATED CONTENT

Supporting Information

The Supporting Information is available free of charge at https://pubs.acs.org/doi/10.1021/acsnano.4c18288.

SEM and TEM images of MoS_2/CNT, TEM images of IrO_2/CNT, XPS survey for the different samples, UV/vis diffuse reflections, band gap energy results of MoS_2/CNT and IrO_2/CNT, Mott−Schottky plots, XPS valence band spectra, LSV curves of different catalysts for HER, contact angles of the catalyst surfaces of IrO_2/MoS_2/CNT and IrO_2/CNT and MoS_2/CNT, CV curves for different electrodes, multistep chronopotentiometric curve for the IrO_2/MoS_2/CNT electrode, analysis of IrO_2/MoS_2/CNT and IrO_2 by the Laviron equation, LSV curves for IrO_2/MoS_2/CNT and IrO_2 and IrO_2/CNT in 0.5 M H_2SO_4 under both methanol-containing and methanol-free environments, Nyquist plots, Bode phase plots, Arrhenius plots, computational models, OER process of adsorption at each step, and HER process of the model at the *H adsorption step (PDF)

AUTHOR INFORMATION

Corresponding Authors

Xuemei Zhou − *Key Laboratory of Carbon Materials of Zhejiang Province, Institute of Industrial Carbon Materials and Hydrogen Energy Technology of Wenzhou University, Wenzhou University, Wenzhou 325035, China;* orcid.org/0000-0002-6264-6603; Email: zxm.mei@163.com

Wei Gao − *State Key Laboratory of Solidification Processing, School of Materials Science and Engineering, Northwestern Polytechnical University, Xi'an 710072, China;* orcid.org/0000-0001-7606-7402; Email: wei.gao@nwpu.edu.cn

Zhi Yang − *Key Laboratory of Carbon Materials of Zhejiang Province, Institute of Industrial Carbon Materials and Hydrogen Energy Technology of Wenzhou University, Wenzhou University, Wenzhou 325035, China;* orcid.org/0000-0002-9265-5041; Email: yang201079@126.com

Authors

Shougang Sun − *Key Laboratory of Carbon Materials of Zhejiang Province, Institute of Industrial Carbon Materials and Hydrogen Energy Technology of Wenzhou University, Wenzhou University, Wenzhou 325035, China*

Ziqi Wan − *State Key Laboratory of Solidification Processing, School of Materials Science and Engineering, Northwestern Polytechnical University, Xi'an 710072, China*

Yingying Xu − *Key Laboratory of Carbon Materials of Zhejiang Province, Institute of Industrial Carbon Materials and Hydrogen Energy Technology of Wenzhou University, Wenzhou University, Wenzhou 325035, China*

Jinjie Qian − *Key Laboratory of Carbon Materials of Zhejiang Province, Institute of Industrial Carbon Materials and Hydrogen Energy Technology of Wenzhou University, Wenzhou University, Wenzhou 325035, China;* orcid.org/0000-0002-9996-7929

Jie Gao − *School of Life Sciences, Northwestern Polytechnical University, Xi'an 710072, China*

Dong Cai − *Key Laboratory of Carbon Materials of Zhejiang Province, Institute of Industrial Carbon Materials and Hydrogen Energy Technology of Wenzhou University, Wenzhou University, Wenzhou 325035, China;* orcid.org/0000-0002-8775-3480

Yongjie Ge − *Key Laboratory of Carbon Materials of Zhejiang Province, Institute of Industrial Carbon Materials and Hydrogen Energy Technology of Wenzhou University, Wenzhou University, Wenzhou 325035, China;* orcid.org/0000-0002-2959-2914

https://doi.org/10.1021/acsnano.4c18288
ACS Nano XXXX, XXX, XXX−XXX

Huagui Nie − *Key Laboratory of Carbon Materials of Zhejiang Province, Institute of Industrial Carbon Materials and Hydrogen Energy Technology of Wenzhou University, Wenzhou University, Wenzhou 325035, China*

Complete contact information is available at: https://pubs.acs.org/10.1021/acsnano.4c18288

Author Contributions

This work represents a collaborative effort with all coauthors participating in manuscript preparation. The final version received unanimous endorsement from all contributors.

Notes

The authors declare no competing financial interest.

ACKNOWLEDGMENTS

Financial support was provided through the National Natural Science Foundation of China (Grant Nos. 22109119), the Natural Science Foundation of Zhejiang Province (LQ24B030009), and the General Scientific Research program of Zhejiang Education Department (Y202352098).

REFERENCES

(1) Song, J.; Wei, C.; Huang, Z.-F.; Liu, C.; Zeng, L.; Wang, X.; Xu, Z. J. A review on fundamentals for designing oxygen evolution electrocatalysts. *Chem. Soc. Rev.* **2020**, *49*, 2196−2214.

(2) Jiao, Y.; Zheng, Y.; Jaroniec, M. T.; Qiao, S. Z. Design of electrocatalysts for oxygen- and hydrogen-involving energy conversion reactions. *Chem. Soc. Rev.* **2015**, *44*, 2060−2086.

(3) McCrory, C. C. L.; Jung, S.; Ferrer, I. M.; Chatman, S. M.; Peters, J. C.; Jaramillo, T. F. Benchmarking Hydrogen Evolving Reaction and Oxygen Evolving Reaction Electrocatalysts for Solar Water Splitting Devices. *J. Am. Chem. Soc.* **2015**, *137*, 4347−4357.

(4) Zhan, Y.; Zhou, X.; Nie, H.; Xu, X.; Zheng, X.; Hou, J.; Duan, H.; Huang, S.; Yang, Z. Designing Pd/O co-doped MoS x for boosting the hydrogen evolution reaction. *J. Mater. Chem. A* **2019**, *7*, 15599−15606.

(5) Wang, S.; Zhang, D.; Li, B.; Zhang, C.; Du, Z.; Yin, H.; Bi, X.; Yang, S. Ultrastable In-Plane 1T−2H MoS_2 Heterostructures for Enhanced Hydrogen Evolution Reaction. *Adv. Energy Mater.* **2018**, *8*, No. 1801345.

(6) Kappera, R.; Voiry, D.; Yalcin, S. E.; Branch, B.; Gupta, G.; Mohite, A. D.; Chhowalla, M. Phase-engineered low-resistance contacts for ultrathin MoS_2 transistors. *Nat. Mater.* **2014**, *13*, 1128−1134.

(7) Li, H.; Tsai, C.; Koh, A. L.; Cai, L.; Contryman, A. W.; Fragapane, A. H.; Zhao, J.; Han, H. S.; Manoharan, H. C.; Abild-Pedersen, F. Activating and optimizing MoS_2 basal planes for hydrogen evolution through the formation of strained sulphur vacancies. *Nat. Mater.* **2016**, *15*, 48−53.

(8) Lin, Y. C.; Dumcenco, D. O.; Huang, Y. S.; Suenaga, K. Atomic mechanism of the semiconducting-to-metallic phase transition in single-layered MoS_2. *Nat. Nanotechnol.* **2014**, *9*, 391−396.

(9) Luo, Z.; Ouyang, Y.; Zhang, H.; Xiao, M.; Ge, J.; Jiang, Z.; Wang, J.; Tang, D.; Cao, X.; Liu, C. Chemically activating MoS_2 via spontaneous atomic palladium interfacial doping towards efficient hydrogen evolution. *Nat. Commun.* **2018**, *9*, 2120.

(10) Benson, E. E.; Zhang, H.; Schuman, S. A.; Nanayakkara, S. U.; Bronstein, N. D.; Ferrere, S.; Blackburn, J. L.; Miller, E. M. Balancing the hydrogen evolution reaction, surface energetics, and stability of metallic MoS_2 nanosheets via covalent functionalization. *J. Am. Chem. Soc.* **2018**, *140*, 441−450.

(11) Jiao, Y.; Mukhopadhyay, A.; Ma, Y.; Yang, L.; Hafez, A. M.; Zhu, H. Ion transport nanotube assembled with vertically aligned metallic MoS_2 for high rate lithium-ion batteries. *Adv. Energy Mater.* **2018**, *8*, No. 1702779.

(12) Zhang, J.; Wang, T.; Pohl, D.; Rellinghaus, B.; Dong, R.; Liu, S.; Zhuang, X.; Feng, X. Interface engineering of MoS_2/Ni_3S_2 heterostructures for highly enhanced electrochemical overall-water-splitting activity. *Angew. Chem. Int. Ed.* **2016**, *128*, 6814−6819.

(13) Qi, Y.; Xu, Q.; Wang, Y.; Yan, B.; Ren, Y.; Chen, Z. CO_2-induced phase engineering: protocol for enhanced photoelectrocatalytic performance of 2D MoS_2 nanosheets. *ACS Nano* **2016**, *10*, 2903−2909.

(14) Yu, Y.; Nam, G. H.; He, Q.; Wu, X. J.; Zhang, K.; Yang, Z.; Chen, J.; Ma, Q.; Zhao, M.; Liu, Z.; Ran, F. R.; Wang, X.; Li, H.; Huang, X.; Li, B.; Xiong, Q.; Zhang, Q.; Liu, Z.; Gu, L.; Du, Y.; Huang, W.; Zhang, H. High phase-purity 1T′-MoS_2- and 1T′-$MoSe_2$-layered crystals. *Nat. Chem.* **2018**, *10*, 638−643.

(15) Wang, J.; Ni, M.; Qian, J.; Ge, Y.; Cai, D.; Nie, H.; Zhou, X.; Yang, Z. Ultrafine Ir nanoparticles anchored on carbon nanotubes as efficient bifunctional oxygen catalysts for Zn−air batteries. *Chem. Commun.* **2024**, *60*, 6415−6418.

(16) Jin, Y.; Huo, W.; Zhou, X.; Zhang, L.; Li, Y.; Yang, S.; Qian, J.; Cai, D.; Ge, Y.; Yang, Z. IrO_2-Stablized La_2IrO_6 perovskite nanotubes via corner-shared interconnections as highly-efficient oxygen evolution electrocatalysts. *Chem. Commun.* **2023**, *59*, 183−186.

(17) Henkelman, G.; Arnaldsson, A.; Jónsson, H. A fast and robust algorithm for Bader decomposition of charge density. *Comput. Mater. Sci.* **2006**, *36*, 354−360.

(18) Liu, G.; Cheng, Y.; Qiu, M.; Li, C.; Bao, A.; Sun, Z.; Yang, C.; Liu, D. Facilitating interface charge transfer via constructing NiO/$NiCo_2O_4$ heterostructure for oxygen evolution reaction under alkaline conditions. *J. Colloid Interface Sci.* **2023**, *643*, 214−222.

(19) Liu, Y.; Chen, Y.; Tian, Y.; Sakthivel, T.; Liu, H.; Guo, S.; Zeng, H.; Dai, Z. Synergizing Hydrogen Spillover and Deprotonation by the Internal Polarization Field in a $MoS_2/NiPS_3$ Vertical Heterostructure for Boosted Water Electrolysis. *Adv. Mater.* **2022**, *34*, No. 2203615.

(20) Liu, J.; Jia, Y.; Ji, L.; Bandaru, S.; Bai, G.; Cheepurupalli, K. K.; Zhang, X. Study of Al-Doped and Al_2O_3 Heterostructures for Improving α-Fe_2O_3 Catalysis for the Oxygen Evolution Reaction. *J. Phys. Chem. C* **2023**, *127*, 8342−8351.

(21) Zhang, W.; Yang, L.; Li, Z.; Nie, G.; Cao, X.; Fang, Z.; Wang, X.; Ramakrishna, S.; Long, Y.; Jiao, L. Regulating Hydrogen/Oxygen Species Adsorption via Built-in Electric Field-Driven Electron Transfer Behavior at the Heterointerface for Efficient Water Splitting. *Angew. Chem. Int. Ed.* **2024**, *63*, No. e202400888.

(22) Fu, S.; Ma, Y.; Yang, X.; Yao, X.; Jiao, Z.; Cheng, L.; Zhao, P. Defect and interface engineering of hexagonal $Fe_2O_3/ZnCo_2O_4$ n-n heterojunction for efficient oxygen evolution reaction. *Appl. Catal., B* **2023**, *333*, No. 122813.

(23) Miao, Z.; Wang, Q.; Zhang, Y.; Meng, L.; Wang, X. In situ construction of S-scheme AgBr/BiOBr heterojunction with surface oxygen vacancy for boosting photocatalytic CO_2 reduction with H_2O. *Appl. Catal., B* **2022**, *301*, No. 120802.

(24) Wang, X.; Qin, Z.; Qian, J.; Chen, L.; Shen, K. IrCo Nanoparticles Encapsulated with Carbon Nanotubes for Efficient and Stable Acidic Water Splitting. *ACS Catal.* **2023**, *13*, 10672−10682.

(25) Kumar, A.; Gil-Sepulcre, M.; Lee, J.; Bui, V. Q.; Wang, Y.; Rüdiger, O.; Kim, M. G.; DeBeer, S.; Tüysüz, H. Iridium Single-Atom-Ensembles Stabilized on Mn-Substituted Spinel Oxide for Durable Acidic Water Electrolysis. *Adv. Mater.* **2024**, *36*, No. 2401648.

(26) Wang, L.; Zhang, C.; Cao, Z.; Zeng, G.; Liu, J.; Ye, S. Dual Modulation of Bulk Electronic Structure and Surficial Active Sites in Sea Urchin-Like MoO_2 Nanoreactors Promoting Electrocatalytic Hydrogen Evolution. *Adv. Funct. Mater.* **2024**, *34*, No. 2406670.

(27) Zhang, L.; Bai, J.; Zhang, S.; Liu, Y.; Ye, J.; Fan, W.; Debroye, E.; Liu, T. Atomically dispersed iridium on polyimide support for acidic oxygen evolution. *ACS Nano* **2024**, *18*, 22095−22103.

(28) Hua, K.; Li, X.; Rui, Z.; Duan, X.; Wu, Y.; Yang, D.; Li, J.; Liu, J. Integrating atomically dispersed ir sites in $MnCo_2O_{4.5}$ for highly stable acidic oxygen evolution reaction. *ACS Catal.* **2024**, *14*, 3712−3724.

(29) Zhu, Y.; Wang, J.; Koketsu, T.; Kroschel, M.; Chen, J. M.; Hsu, S. Y.; Henkelman, G.; Hu, Z.; Strasser, P.; Ma, J. Iridium single atoms

incorporated in Co_3O_4 efficiently catalyze the oxygen evolution in acidic conditions. *Nat. Commun.* **2022**, *13*, 7754.
(30) Ding, H.; Su, C.; Wu, J.; Lv, H.; Tan, Y.; Tai, X.; Wang, W.; Zhou, T.; Lin, Y.; Chu, W. Highly Crystalline Iridium−Nickel Nanocages with Subnanopores for Acidic Bifunctional Water Splitting Electrolysis. *J. Am. Chem. Soc.* **2024**, *146*, 7858−7867.
(31) Jin, Y.; Huo, W.; Zhang, L.; Li, Y.; Chen, Q.; Zhang, X.; Yang, S.; Nie, H.; Zhou, X.; Yang, Z. $NaBH_4$-reduction induced tunable oxygen vacancies in $LaNiO_{2.7}$ to enhance the oxygen evolution reaction. *Chem. Commun.* **2021**, *57*, 7168−7171.
(32) Huo, W.; Zhou, X.; Jin, Y.; Xie, C.; Yang, S.; Qian, J.; Cai, D.; Ge, Y.; Qu, Y.; Nie, H.; Yang, Z. Rhenium suppresses Iridium (IV) oxide crystallization and enables efficient, stable electrochemical water oxidation. *Small* **2023**, *19*, No. 2207847.
(33) Gou, W.; Zhang, M.; Zou, Y.; Zhou, X.; Qu, Y. Iridium-Chromium Oxide Nanowires as Highly Performed OER Catalysts in Acidic Media. *ChemCatChem.* **2019**, *11*, 6008−6014.
(34) Xiao, Z.; Huang, Y.-C.; Dong, C.-L.; Xie, C.; Liu, Z.; Du, S.; Chen, W.; Yan, D.; Tao, L.; Shu, Z.; Zhang, G.; Duan, H.; Wang, Y.; Zou, Y.; Chen, R.; Wang, S. Operando Identification of the Dynamic Behavior of Oxygen Vacancy-Rich Co_3O_4 for Oxygen Evolution Reaction. *J. Am. Chem. Soc.* **2020**, *142*, 12087−12095.
(35) Chen, W.; Wu, B.; Wang, Y.; Zhou, W.; Li, Y.; Liu, T.; Xie, C.; Xu, L.; Du, S.; Song, M.; Wang, D.; Liu, Y.; Li, Y.; Liu, J.; Zou, Y.; Chen, R.; Chen, C.; Zheng, J.; Li, Y.; Chen, J.; Wang, S. Deciphering the alternating synergy between interlayer Pt single-atom and NiFe layered double hydroxide for overall water splitting. *Energy Environ. Sci.* **2021**, *14*, 6428−6440.
(36) Su, H.; Zhou, W.; Zhou, W.; Li, Y.; Zheng, L.; Zhang, H.; Liu, M.; Zhang, X.; Sun, X.; Xu, Y. In-situ spectroscopic observation of dynamic-coupling oxygen on atomically dispersed iridium electrocatalyst for acidic water oxidation. *Nat. Commun.* **2021**, *12*, 6118.
(37) Yang, C.; Zhang, X.; An, Q.; Liu, M.; Zhou, W.; Li, Y.; Hu, F.; Liu, Q.; Su, H. Dynamically-evolved surface heterojunction in iridium nanocrystals boosting acidic oxygen evolution and overall water splitting. *J. Energy Chem.* **2023**, *78*, 374−380.
(38) Sun, Q.; Liu, J.; Ji, X.; Chen, D.; Guo, Y.; Mao, L.; Qian, J. Metal-organic framework derived hollow nitrogen-doped carbon sphere with cobalt phosphide in carbon nanotube for efficient oxygen evolution. *J. Colloid Interface Sci.* **2023**, *652*, 1338−1346.
(39) Huang, J.; Sheng, H.; Ross, R. D.; Han, J.; Wang, X.; Song, B.; Jin, S. Modifying redox properties and local bonding of Co_3O_4 by CeO_2 enhances oxygen evolution catalysis in acid. *Nat. Commun.* **2021**, *12*, 3036.
(40) Zhao, B.; Liu, J.; Xu, C.; Feng, R.; Sui, P.; Wang, L.; Zhang, J.; Luo, J.; Fu, X. Hollow NiSe Nanocrystals Heterogenized with Carbon Nanotubes for Efficient Electrocatalytic Methanol Upgrading to Boost Hydrogen Co-Production. *Adv. Funct. Mater.* **2021**, *31*, No. 2008812.
(41) Kari, J.; Olsen, J. P.; Jensen, K.; Badino, S. F.; Krogh, K. B. R. M.; Borch, K.; Westh, P. Sabatier Principle for Interfacial (Heterogeneous) Enzyme Catalysis. *ACS Catal.* **2018**, *8*, 11966−11972.
(42) Yu, J.; Li, J.; Xu, C. Y.; Li, Q.; Liu, Q.; Liu, J.; Chen, R.; Zhu, J.; Wang, J. Modulating the d-band centers by coordination environment regulation of single-atom Ni on porous carbon fibers for overall water splitting. *Nano Energy* **2022**, *98*, No. 107266.
(43) Wang, C.; Yu, L.; Yang, F.; Feng, L. MoS_2 nanoflowers coupled with ultrafine Ir nanoparticles for efficient acid overall water splitting reaction. *J. Energy Chem.* **2023**, *87*, 144−152.
(44) Greeley, J.; Jaramillo, T. F.; Bonde, J.; Chorkendorff, I.; Nørskov, J. K. Computational high-throughput screening of electrocatalytic materials for hydrogen evolution. *Nat. Mater.* **2006**, *5*, 909−913.
(45) Tan, C.; Luo, Z.; Chaturvedi, A.; Cai, Y.; Du, Y.; Gong, Y.; Huang, Y.; Lai, Z.; Zhang, X.; Zheng, L.; Qi, X.; Goh, M. H.; Wang, J.; Han, S.; Wu, X.; Gu, L.; Kloc, C.; Zhang, H. Preparation of High-Percentage 1T-Phase Transition Metal Dichalcogenide Nanodots for Electrochemical Hydrogen Evolution. *Adv. Mater.* **2018**, *30*, No. 1705509.
(46) Yue, D.; Feng, T.; Zhu, Z.; Lu, S.; Yang, B. Ir single atom-doped Ni_2P anchored by carbonized polymer dots for robust overall water splitting. *ACS Catal.* **2024**, *14*, 3006−3017.
(47) Chen, Y.; Liu, Y.; Li, L.; Sakthive, T.; Guo, Z.; Dai, Z. Asymmetric Bond Delta-Polarization at the Interfacial Se-Ru-O Bridge for Efficient pH-Robust Water Electrolysis. *Adv. Funct. Mater.* **2024**, *34*, No. 2406587.
(48) Wang, H.; Chen, Z. n.; Wang, Y.; Wu, D.; Cao, M.; Sun, F.; Cao, R. Sub-10-nm-sized Au@ Au_xIr_{1-x} metal-core/alloy-shell nanoparticles as highly durable catalysts for acidic water splitting. *Natl.Sci. Rev.* **2024**, *11*, No. nwae056.
(49) Kresse, G.; Furthmüller, J. Efficient iterative schemes for ab initio total-energy calculations using a plane-wave basis set. *Phys. Rev. B* **1996**, *54*, 11169.
(50) Perdew, J. P.; Burke, K.; Ernzerhof, M. Generalized Gradient Approximation Made Simple. *Phys. Rev. Lett.* **1996**, *77*, 3865−3868.
(51) Blöchl, P. E. Projector augmented-wave method. *Phys. Rev. B* **1994**, *50*, 17953−17979.
(52) Monkhorst, H. J.; Pack, J. D. Special points for Brillouin-zone integrations. *Phys. Rev. B* **1976**, *13*, 5188.
(53) Nørskov, J. K.; Rossmeisl, J.; Logadottir, A.; Lindqvist, L.; Kitchin, J. R.; Bligaard, T.; Jónsson, H. Origin of the Overpotential for Oxygen Reduction at a Fuel-Cell Cathode. *J. Phys. Chem. B* **2004**, *108*, 17886−17892.

https://doi.org/10.1021/acsnano.4c18288
ACS Nano XXXX, XXX, XXX−XXX